Polymer Chemistry

ROYAL SOCIETY OF CHEMISTRY

PAPER

View Article Online
View Journal | View Issue

Check for updates

**Cite this:** *Polym. Chem.*, 2026, **17**, 476

# From spheres to worms to vesicles: kinetic control of nanostructure formation from the same block copolymer

Juliane Eberhardt,[a,b] Stephanie Hoeppener, [c,d] Ulrich Mansfeld[b] and Johannes C. Brendel *[a,b]

Received 2nd November 2025,
Accepted 15th December 2025

DOI: 10.1039/d5py01038a

rsc.li/polymers

Block copolymer self-assembly in solution offers a versatile platform for designing nanostructures with tailored morphologies in aqueous environments. While morphology is commonly controlled by adjusting block ratios, kinetic trapping of nanostructures represents a powerful yet underexplored strategy to direct shape and structure formation, for example in biomedical applications. In this study, we investigate the self-assembly behavior of the amphiphilic block copolymer poly[(butyl acrylate)$_{50}$-*co*-(pyridyl disulfide ethyl acrylate)$_5$]-*block*-(poly ethylene oxide)$_{125}$-N$_3$ (P(BA$_{50}$-PDSA$_5$)-*b*-PEO$_{125}$-N$_3$) using a solvent switch method. The polymer features a neutral, biocompatible hydrophilic block and a hydrophobic block with a low glass transition temperature ($T_g$). By systematically varying the initial solvent composition (DMSO/acetone), polymer concentration (1, 4, 7 mg mL$^{-1}$), and water addition rate (1, 2, 4, 20 mL h$^{-1}$), we demonstrate precise control over nanoparticle morphology. DMSO content above 80% favored vesicle formation, while balanced DMSO/acetone mixtures stabilized worm-like micelles. Lower polymer concentration of 1 mg mL$^{-1}$ resulted in a decrease in the formation of non-spherical morphologies, and faster water addition rate of 4 mL h$^{-1}$ broadened the worm phase, indicating a strong influence of kinetics on the final morphology. Characterization *via* asymmetric flow field-flow fractionation (AF4), dynamic light scattering (DLS), and cryogenic transmission electron microscopy (cryo-TEM) revealed sharp transitions and mixed phases, highlighting the sensitivity of the system to subtle assembly conditions. These findings provide mechanistic insights into morphology control and underscore the potential of kinetically guided self-assembly for designing shape-specific nanostructures, which is particularly relevant for biomedical applications where nanoparticle shape influences biodistribution, cellular uptake, and therapeutic efficacy.

## Introduction

The self-assembly of block copolymers has been a subject of intense research for several decades, and continues to be of great interest due to the broad applicability of the resulting nanostructures. Early studies were enabled by the development of living polymerization techniques, which allowed the synthesis of well-defined block copolymers.[1] The field expanded significantly with the advent of reversible deactivation radical polymerizations, which broadened the scope of accessible monomers.[2–7] Initial efforts focused on understanding the mechanisms of self-assembly and identifying the parameters that govern morphology formation.[8–10] More recently, research has shifted towards designing functional block copolymers for tailor-made applications, thereby expanding the applicability of these nanomaterials in areas like biomedicine, lithography, energy conversion and storage, as well as emulsifiers.[11–18]

Block copolymer self-assembly is driven either by the immiscibility between chemically distinct blocks or insolubility of one block in selective solvents, leading to microphase separation in bulk or formation of nanostructures in solution. The latter structures typically range from 5 to 200 nm in size, showing distinct morphologies, including spheres, worm-like micelles, and vesicles.[19] Despite decades of research, challenges in this field remain, *e.g.*, the targeting of specific morphologies, in particular non-spherical structures,[20–22] and achieving reproducible control over particle morphology.[23] Traditionally, controlled variations in morphology have been accomplished by adjusting the block ratio of the copolymer, thereby tuning the balance between solvophobic and solvophilic interactions.[24,25] Another widely used method is polymeriz-

---

[a] *Macromolecular Chemistry I, University of Bayreuth, Universitätsstr. 30, 95447 Bayreuth, Germany. E-mail: johannes.brendel@uni-bayreuth.de*

[b] *Institute of Macromolecular Research (BIMF) and Bavarian Polymer Institute (BPI), University of Bayreuth, Universitätsstr. 30, 95447 Bayreuth, Germany*

[c] *Laboratory of Organic and Macromolecular Chemistry (IOMC), Friedrich Schiller University Jena, Humboldtstr. 10, 07743 Jena, Germany*

[d] *Jena Center for Soft Matter (JCSM), Friedrich Schiller University Jena, Philosophenweg 7, 07743 Jena, Germany*

ation-induced self-assembly (PISA), where the self-assembly occurs concurrently with the polymerization process, enabling access to a range of morphologies.[26] Nevertheless, kinetic barriers can limit the versatility of structures, restricting the formation of the thermodynamic equilibrium.[27] As a result, only a small number of monomers, which are soluble in water, allow access to the broad variety of morphologies.[28]

The concept of the packing parameter provides a useful, though limited, framework for predicting morphologies. This dimensionless parameter depends on the volume of the hydrophobic block, the effective interfacial area, and the length of the hydrophobic chain.[18,29] While being developed and effective for surfactants, the packing parameter is often insufficient for the prediction of block copolymer assemblies since the chain conformation plays a significant role which limits the precise determination of the specific parameters.[30] As a result, extensive experimental screening is typically necessary to gain a more comprehensive understanding of the resulting morphologies.[31,32]

Moreover, the concept of the packing parameter relies on structures in a thermodynamically favored equilibrium state. The self-assembly of block copolymers in selective solvents, however, can lead to kinetically trapped states, in particular if aqueous solutions are utilized.[33] With increasing amounts of the non-solvent (water), the mobility of the insoluble core blocks decreases. Initially, micelles grow and compact to reduce interfacial energy, but once the core reaches a glassy or highly viscous state, further morphological transitions are hindered or impossible.[24] Rapid kinetic trapping of polymer nanostructures in metastable states, *e.g.*, by quenching the assembly by water, can be a beneficial strategy, particularly when compounds are to be encapsulated in the polymer nanostructure. Possible applications of this approach include *e.g.* the formulation of polymer nanoparticle based drug delivery systems by nanoprecipitation.[34,35] However, this method is limited mainly to the formation of spherical particles with a limited size range.[36] To allow for more morphological variety and better control over the nanostructures, it is more common to dissolve the block copolymer in a non-selective solvent and the selective solvent is added slowly. If the concentration of the solution is above the critical micelle concentration, this causes the solvophobic blocks to aggregate, leading to the formation of micelles. The selective non-solvent is afterwards removed by evaporation or dialysis.[12,37,38] This technique is referred to as the solvent switch method.

In particular, the group of Eisenberg pioneered investigations on the impact of kinetics on the self-assembly behavior.[24,37,39–43] Focusing on highly asymmetric block copolymers with a large polystyrene block and short hydrophilic poly(acrylic acid) blocks, they were able to create spheres, worms or vesicles depending on the addition rate of the water as selective solvent. Several parameters like the concentration of the polymer in solution or the solubility of both blocks in the good solvent and the selective solvent were scrutinized to gain detailed insights into the process. Inspired by these results, subsequent investigations expanded the scope of this methodology towards non-ionic or cationic block polymers and more complex architectures.[44–49] For example, Vena *et al.* utilized $PS_{250}$-*b*-$PEO_{45}$ to perform a series of self-assembly experiments under varying conditions, resulting in spherical particles with distinct surface and internal structure.[46] A common aspect of most of the studied systems is the asymmetric composition of the block copolymer, comprising polystyrene blocks of a rather high degree of polymerization (>100). Furthermore, this hydrophobic block features a high glass transition temperature $T_g$, which has often been considered crucial to trap polymers and decrease their mobility. Although the glass transition has an impact on the chain equilibrium in micelle formation,[50] there have been reports that also low $T_g$ block copolymers can form kinetically trapped or frozen nanostructures,[33,51] which is commonly related to very low critical micelle concentrations and a high surface tension induced by dissolution of the respective hydrophobic blocks.[52,53] Our recent work further demonstrated that it is possible to trap such low $T_g$ block copolymers in different morphologies starting from the same block copolymer.[54] It was demonstrated that spheres, worm-like micelles or vesicles can be created from $P(BA_{50}$-$PDSA_5)$-*b*-$PEO_{125}$-$N_3$, a block copolymer with similar molar masses of both blocks, depending on the organic non-selective solvent used for the solvent switch.

In this study, we investigate the assembly behavior of the selected polymer to evaluate the sensitivity and reproducibility of kinetically controlled nanoparticle formulations. Our objective is to identify the parameters that determine the final nanoparticle shape and to highlight key factors in self-assembly that enable selective and reproducible targeting of specific pure morphologies. We further examine whether similar governing factors can be identified for this symmetric, non-ionic, low-$T_g$ block copolymer, as has previously been reported for highly asymmetric polystyrene block copolymers. Therefore, the ratio of acetone and DMSO in the organic co-solvent was systematically varied, several concentrations of the polymer were tested, and, most importantly, the water addition rate during the solvent switch was altered to determine their impact on the morphology. Understanding the critical parameters that control block copolymer self-assembly is essential for advancing these complex systems toward practical applications, particularly as carriers in biomedical contexts where particle shape and morphology play a decisive role.[21,54]

## Results and discussion

We focused on the amphiphilic block copolymer poly[(butyl acrylate)$_{50}$-*co*-(pyridyl disulfide ethyl acrylate)$_5$]-*block*-(poly ethylene oxide)$_{125}$-$N_3$ ($P(BA_{50}$-$PDSA_5)$-*b*-$PEO_{125}$-$N_3$), which consists of a hydrophobic copolymer composed of butyl acrylate (BA) and pyridyldisulfide ethyl acrylate (PDSA), and a hydrophilic block of polyethyleneoxide (PEO) terminated with an azide group, which can be seen in Fig. 1, for the self-assembly study, which was prepared according to the previously published procedure.[54] NMR and GPC data of the polymer are

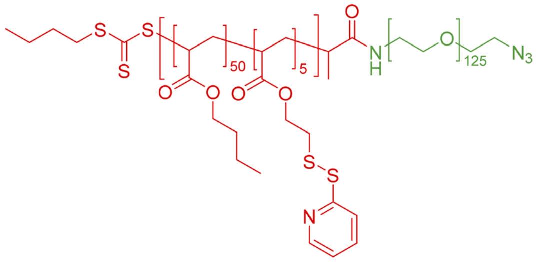

**Fig. 1** Chemical structure of the amphiphilic block copolymer P(BA$_{50}$-PDSA$_5$)-*b*-PEO$_{125}$-N$_3$ used for nanoparticle formation.

shown in Fig. S1 and S2. The PDSA (pyridyldisulfide ethyl acrylate) in the hydrophobic block enables crosslinking of the nanoparticles after their formulation, if required to enhance stability during analysis or for further application.[55,56] The hydrophilic block is made out of poly(ethylene oxide) facilitated with an azide-endgroup allowing further modification with labels or targeting units, which can be useful for further applications. The self-assembly process was induced by the well-established solvent switch process.[57] Therefore, the polymer was first dissolved in acetone, DMSO or a mixture of both before water was continuously added *via* a syringe pump until a ratio of 1 : 1 was reached. This ratio is generally sufficient to induce the self-assembly process of the copolymer. Then, the organic solvent was removed by dialysis before the obtained assembled structures were crosslinked by the addition of 1,6-hexane dithiol, which reacts with the PDSA units. Finally, particles were again dialyzed before characterization.

Our previous studies already revealed that in general three different morphologies (spherical micelles, worm-like micelles, and vesicles) can be formed by this amphiphilic block copolymer.[54] In this study we aimed to elucidate the critical parameters for creating the distinct structures and gain a better understanding and control of the assembly process. Therefore, the effect of (i) the initial concentration of the polymer, (ii) the rate of water addition, and (iii) gradual changes in the initial solvent composition (DMSO/acetone) were examined to determine their respective influence on the morphology (Fig. 2). The concentration of the block copolymer was varied between 1, 4 and 7 mg mL$^{-1}$, while 1, 2 and 4 mL h$^{-1}$ were initially tested as rates of water addition. In all cases, a set of solvent mixtures were applied in the starting solution, which gradually changed from pure acetone to DMSO (in steps of 10%). After crosslinking and purification, all obtained morphologies were analyzed by DLS and AF4 measurements. Selected samples were examined using cryo-TEM investigations.

### Impact of starting solvent composition

As a starting point, we first evaluated the previously established procedure in more detail,[54] focusing on systematic changes of the solvent composition (acetone/DMSO). The solvents were selected based on their miscibility with water and their ability to dissolve both polymer blocks. The initial concentration of the polymer was set to 4 mg mL$^{-1}$ and the water addition rate was kept at 2 mL h$^{-1}$. AF4 measurements revealed significant differences in elution times and the corresponding radii of gyration ($R_g$) at the peak elution time of each nanostructure vary significantly when the solvent composition is changed (summary depicted in Fig. 3a, exemplarily chosen AF4 elugrams are presented in Fig. 3f–i). At high acetone content (DMSO <30%), mostly small particles (<20 nm) are detected, which correspond well to spherical micelles in terms of their size. The AF4 results are further confirmed by DLS measurements (Fig. S3), as the hydrodynamic radii $R_h$ remain below 30 nm. Since all other morphologies are significantly larger in size, following samples with $R_g$ values below 10 nm were considered to be small spherical micelles. At 40% DMSO, a second peak or shoulder appears in the AF4 elugrams indicating the formation of larger structures. In accordance, the corresponding $R_g$ values at this second peak are significantly larger (~100 nm). Additional TEM measure-

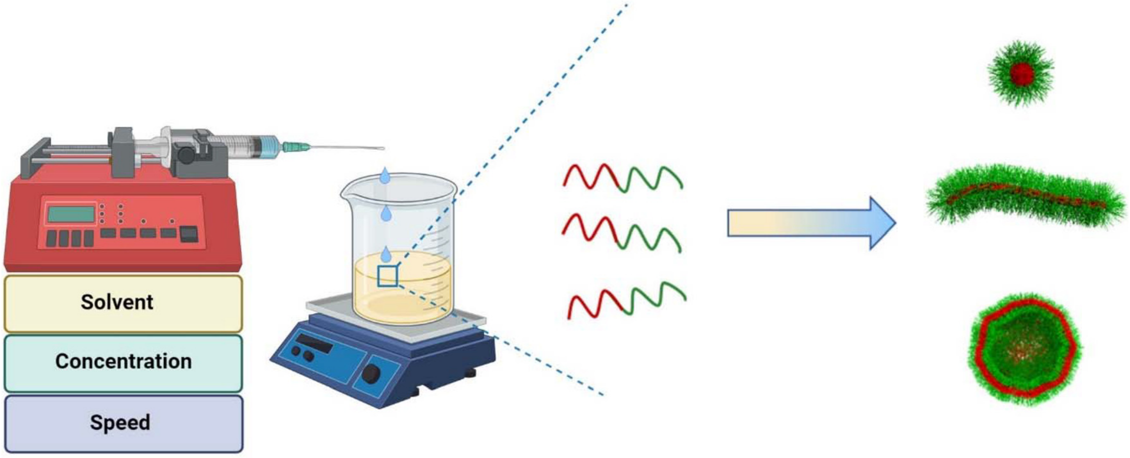

**Fig. 2** Illustrative outline of nanoparticle formulation.

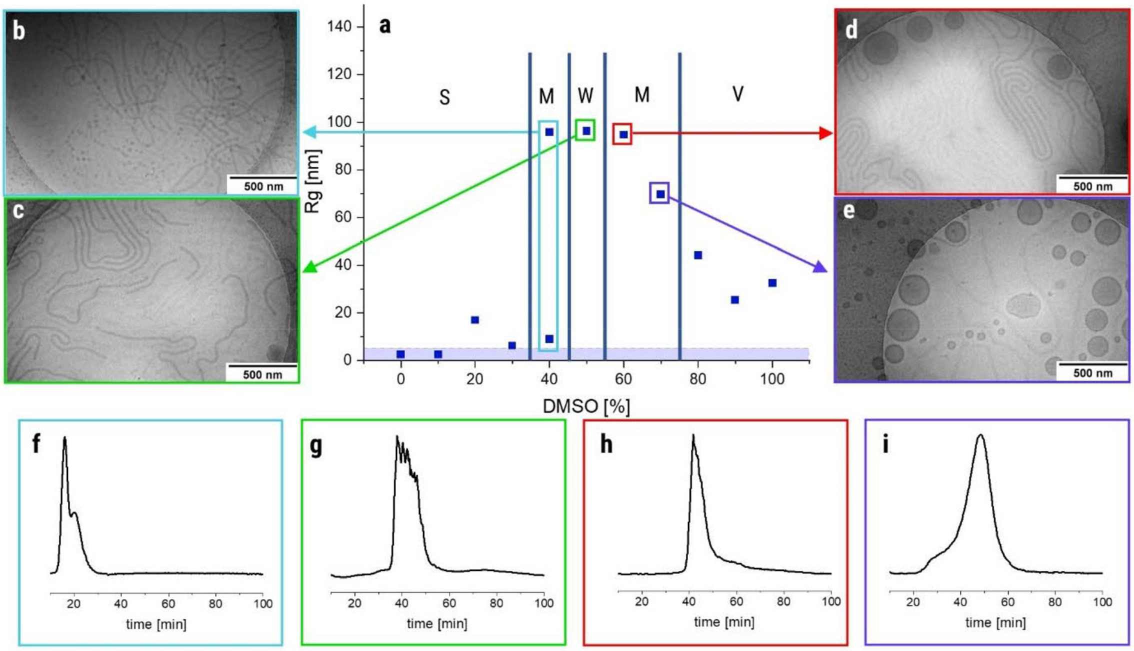

**Fig. 3** Morphological investigations of samples prepared from different starting solvent compositions with increasing DMSO content (100% acetone to 100% DMSO) by AF4 and cryo-TEM. The concentration and water addition rate were kept at 4 mg mL$^{-1}$ and 2 mL h$^{-1}$, respectively. S = spheres, M = mixed morphologies, W = worm-like micelles, V = vesicles. The (a) $R_g$ over solvent ratio. Morphologies were assigned to values based on particle size and microscopy images. (b) Spherical and worm-like micelles at 40% DMSO; (c) worm-like micelles at 50% DMSO; (d) worm-like micelles and a small amount of vesicles at 60% DMSO; (e) vesicles and a small amount of worm-like micelles at 70% DMSO; AF4 elugrams measured with UV detector at 280 nm for (f) 40%; (g) 50%; (h) 60% and (i) 70% DMSO.

ments indeed revealed the presence of both spherical and worm-like micelles in the samples confirming the onset of a morphology transition (Fig. 3b). Interestingly, the next step to 50% DMSO yielded already a pure worm-phase (Fig. 3c) and no more spherical micelles could be observed. The complete transition is also confirmed by the AF4 measurements (Fig. S4), since no signal appears at low elution times (<20 min), which would be representative for spherical micelles. A further increase of the DMSO content to 60% does not appear to induce a major change in the AF4 results, since elution times and the corresponding $R_g$ do not change significantly (Fig. 3h). However, TEM images revealed already the presence of several vesicles besides the observed worm-like micelles (Fig. 3d). Increasing the DMSO content in the initial solvent mixture further, the ratio of vesicles in the mixture increases (Fig. 3e) and concomitantly the elution times shift towards higher values (Fig. 3i), although the shift is not as clear as for the transition between spherical and worm-like micelles. The corresponding $R_g$ values also decrease, which is related to the smaller radii of gyration for round vesicles compared to the highly elongated worm-like micelles. Consequently, the presence of a pure vesicle phase can be assigned at contents of 80% DMSO and higher (Fig. S5).

These results clearly illustrate that small changes in the starting solvent composition have already a major impact on resulting morphologies. Nevertheless, all major morphologies can be obtained as pure phases, although a broader transition range is present between worm-like micelles and vesicles. In this case, it is difficult to find out which morphology is thermodynamically favored. One possible hint would be the transition of thermodynamically non-favored morphologies over long periods of time.[58] Therefore, a sample of non-cross-linked worm-like micelles, which are assumed as thermodynamically less stable morphologies due to its rare occurrence, was measured in AF4 again after one year at room temperature. The resulting elugram showed only a slight shift but no significant change of the peak shape, that is common for worm-like micelles, or the $R_g$ value, which was 75.2 nm directly after assembly and 76.7 nm after 1 year of storage (Fig. S6). To have a closer look on the thermodynamic stability of all morphologies, non-crosslinked samples were kept at 80 °C for one week, which should enhance dynamics in the system.[59] No significant changes in their size were observed and the morphologies seem preserved (Fig. S7). Hence, it is difficult to judge on the thermodynamically favored morphology of the system.

## Influence of the initial concentration of the polymer

After revealing the impact of the solvent composition, we further expanded the parameter space by varying the initial concentration of the block copolymer in the organic solvent mixture. A lower (1 mg mL$^{-1}$) and a higher (7 mg mL$^{-1}$) concentration were tested and compared to the initially applied concentration of 4 mg mL$^{-1}$. The initial concentration of 4 mg mL$^{-1}$ was chosen to provide sufficiently concentrated samples for application in the Ussing chamber experiments reported previously.[54] The now tested concentrations were selected to ensure that the polymer remains fully dissolved without aggregation for 7 mg mL$^{-1}$, while the final samples prepared from 1 mg mL$^{-1}$ still provide a reliable signal in AF4 measurements without need for further treatment. In both cases, the same stepwise change in the solvent composition was applied in order to detect changes in the phase transitions (Fig. 4a and b). TEM-images were made for the batches with 50% and 80% DMSO to confirm the predicted morphologies (Fig. 4d and e).

At a lower concentration (1 mg mL$^{-1}$), the composition range has expanded up to 60% of DMSO, where pure spherical micelles are formed. At 70% DMSO a slight increase of particle size was observed indicating a morphological transition. Interestingly, cryo-TEM analysis of this sample revealed that mainly small vesicles were formed and only few worm-like micelles can be observed (Fig. 4c). When increasing the DMSO content further, the peaks in the AF4 measurement become more narrow and lower $R_g$ values are obtained, which indicates the formation of only vesicles (Fig. S4, S9 and S11). Those vesicles have an $R_g$ of approximately 25 nm, which are smaller in comparison to vesicles which are formed at higher concentrations (4 mg mL$^{-1}$). This trend was found as well when comparing the particles in DLS measurements (Fig. S3, S8 and S10). The decreased concentration in general has a significant impact on the formation of different morphologies. The formation of worm-like micelles is nearly completely impeded at low polymer concentrations. We assume that the worm-like micelles are formed by fusion of first aggregates,[60] which only can take place if their concentration is high enough. At this low concentration the formation of spherical micelles prevails, while at high DMSO levels the process switches directly to the vesicle formation. This straight transition indicates that the vesicles are emerging from individual nucleates rather than form by fusion of particles. This fundamentally important aspect deserves attention in subsequent studies. These require more sophisticated kinetic experiments to identify the exact mechanism, which was beyond the scope of this study.[24,39]

Based on these results, we assumed that an increase of the polymer concentration might broaden the range where worm-like micelles are formed. However, the results of the AF4 measurements reveal a very similar picture for 7 mg mL$^{-1}$ (Fig. 4b) as observed for the experiments with 4 mg mL$^{-1}$ (Fig. 3a). Again, a broad transition between worm-like micelles and vesicles is observed, but no significant shift of the phase. Only the size of the obtained nanostructures appears increased when comparing the $R_g$ values and the results of the DLS measurements for nanoparticles at different concentrations. Vesicles formed in pure DMSO at different concentrations were compared, revealing that the vesicles with the lowest concentration (1 mg mL$^{-1}$) had an $R_g$ of 25.2 nm. At a concen-

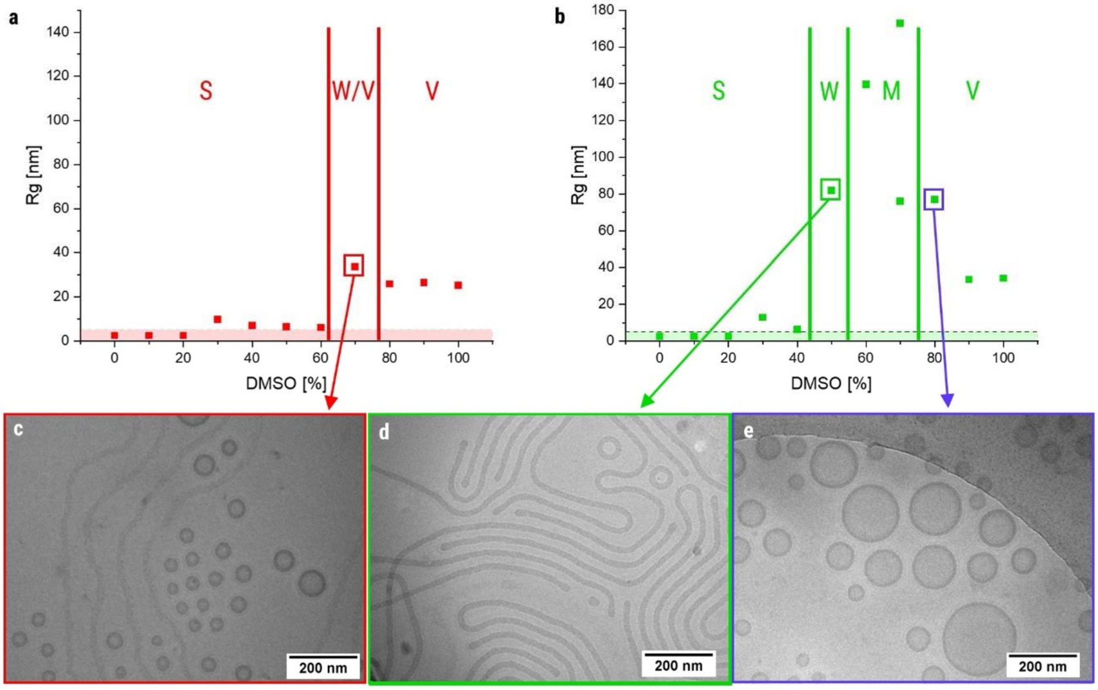

**Fig. 4** Morphological investigations about the influence of initial polymer concentration. $R_g$ over DMSO ratio which was used for solvent switch procedure with initial polymer concentration of (a) 1 mg mL$^{-1}$ and (b) 7 mg mL$^{-1}$. Water addition rate was kept at 2 mL h$^{-1}$. Morphologies were assigned to values based on particle size and cryo-TEM images. S = spheres, W = worm-like micelles, V = vesicles, M = mixed morphologies. Cryo-TEM images of (c) 1 mg mL$^{-1}$, 70% DMSO (worm-like micelles and small vesicles); (d) 7 mg mL$^{-1}$, 50% DMSO (predominantly worm-like micelles); (e) 7 mg mL$^{-1}$, 80% DMSO (vesicles).

tration of 4 mg mL$^{-1}$, the $R_g$ increased to 32.6 nm. The largest vesicles, with an $R_g$ of 34.2 nm, were observed at a concentration of 7 mg mL$^{-1}$. This observation was also reported by Eisenberg *et al.*,[24] who found that an increase in concentration leads to a corresponding increase in the aggregation number. This leads to larger micelle cores and to a higher degree of stretching of the hydrophobic block, which is in our case butyl acrylate. However, the general assembly process seems not to be influenced by the increased concentration and other factors appear to be more critical in this regard.

### Varying the rate of water addition

Besides the polymer concentration, we also considered the time for the polymers to assemble a critical factor. In this regard, we varied the rate at which the water is added to the polymer solution in the different solvent mixtures. Using an initial addition rate of 2 mL h$^{-1}$, we now tested a lower rate (1 mL h$^{-1}$) and a higher rate (4 mL h$^{-1}$).

In all cases, the transition from small particles (most likely small spherical micelles) to worm-like micelles occurred at 40% to 50% DMSO content (Fig. 5a–c). This transition seems therefore determined by the solvent composition and cannot be affected by the other tested parameters. However, the second transition between worm-like micelles and vesicles appears more sensitive to changes in the water addition rate. While at slower addition rates of 1 mL h$^{-1}$ and 2 mL h$^{-1}$, the pure worm-like micelle phase is only observed at 50% DMSO, at 4 mL h$^{-1}$, this phase is extended up to 70% DMSO in the initial solvent mixture compared to the slower addition rates. Additionally, at 2 mL h$^{-1}$, a broader range of mixed morphologies, including worm-like micelles and vesicles, is observed compared to 1 mL h$^{-1}$. The shift of the transition point is best illustrated in the cryo-TEM images recorded from batches prepared at a solvent mixture of 70% DMSO and 30% acetone and different water addition rates (Fig. 5d–f). While at 1 mL h$^{-1}$ only vesicles are formed, an increase to 2 mL h$^{-1}$ already causes a mixed phase of worm-like micelles and vesicles and speeding the addition further up provides a pure phase of worm-like micelles. Interestingly, at this rate the change to 80% DMSO in the starting solvent appears to induce a straight transition towards vesicles considering the narrow distribution observed in AF4 measurements and the decrease of $R_g$ values. AF4 measurements also confirmed a broader worm phase at 4 mL h$^{-1}$, as evidenced by the irregular peak shape observed when non-spherical particles are measured (Fig. S4, S13 and S15). DLS measurements of samples with different water addition rates can be seen in Fig. S3, S12 and S14. The increase of the addition rate therefore narrows down the transition range, where mixed structures are obtained, and thus this parameter represents a critical factor to ensure pure morphologies, which are often desired. Overall, the assembly process appears to be kinetically driven, although the influence of the water addition rate is not as significant as for the previously reported asymmetric polystyrene block copolymers.[39] At lower addition rates, competing processes forming either worm-like micelles or vesicles can still occur in parallel. However, increasing the rate discriminates one process over the other and thus causes selection.

Intrigued by this observation, we expanded the study and tested a much higher water addition rate of 20 mL h$^{-1}$. To our surprise, the AF4 measurements (Fig. S17) indicated a change in the structures at much lower DMSO contents of around

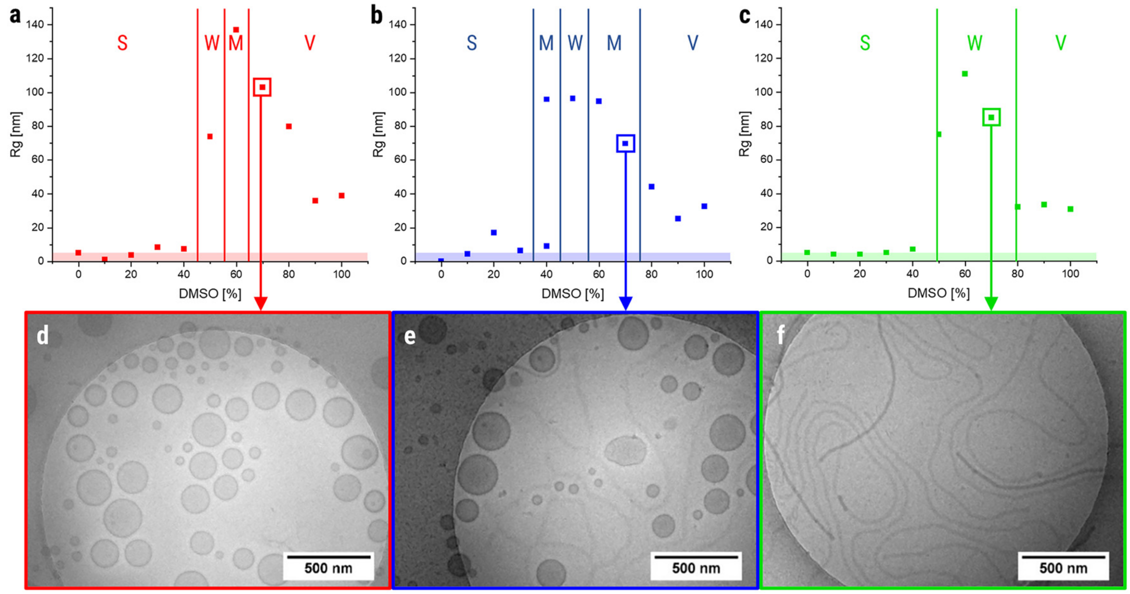

**Fig. 5** Morphological investigations about the influence of water addition rate. $R_g$ over DMSO content which was used for solvent switch procedure with (a) 1 mL h$^{-1}$, (b) 2 mL h$^{-1}$ and (c) 4 mL h$^{-1}$ water addition speed. Initial polymer concentration was kept at 4 mg mL$^{-1}$. Cryo-TEM images of different batches with different water addition speed with solvent ratio of 70 : 30 DMSO : acetone revealed the presence of (d) vesicles (1 mL h$^{-1}$); (e) worm-like micelles and vesicles (2 mL h$^{-1}$); (f) worm-like micelles (4 mL h$^{-1}$).

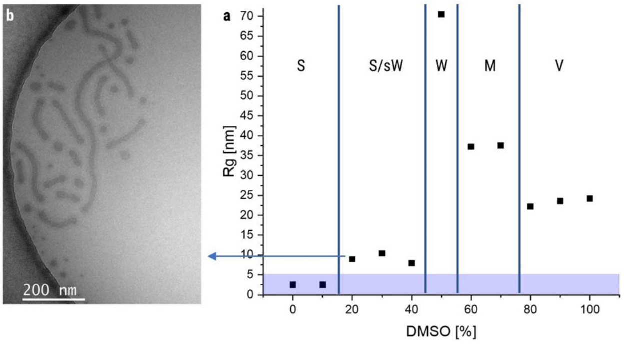

**Fig. 6** (a) $R_g$ over DMSO content which was used for solvent switch procedure for an initial polymer concentration of 4 mg $mL^{-1}$ and a water addition rate of 20 mL $h^{-1}$. Morphologies were assigned to values based on particle size and cryo-TEM images. S = spheres, sW = small worm-like micelles, W = worm-like micelles, M = mixed morphologies, V = vesicles; (b) Cryo-TEM image for 20% DMSO showing short worm-like micelles besides spherical micelles.

20%, which before led in every case to the formation of pure spherical micelles. At this high addition rate, the $R_g$ increased between 10% and 20% DMSO (Fig. 6a). Cryo-TEM measurements (Fig. 6b) indeed revealed that for 20 mL $h^{-1}$ and 20% DMSO already short worm-like micelles (~150 nm) were formed besides the expected spherical micelles. Surprisingly, those short worms did not show an irregular peak shape in AF4, this seems to arise only for longer worm-like micelles. However, only at 50% and more DMSO content again worm-like micelles of length >1 μm were obtained. DLS measurements for those samples can be seen in Fig. S16. The mechanism inducing the formation of short worm-like micelles at very low DMSO content remains unclear, but it has to be kept in mind that the high addition rate (1 mL is added in only 3 min) turbulences in the vial might cause additional aggregation and inhomogeneities may enhance the aggregation of first particles. A better control of the mixing process might provide a clearer picture of the impact of such high addition rates and experiments using microfluidics are currently being developed.

## Conclusion

In this study, we systematically investigated the self-assembly behavior of the amphiphilic block copolymer $P(BA_{50}\text{-}PDSA_5)\text{-}b\text{-}PEO_{125}\text{-}N_3$ using a solvent switch method. By varying the solvent composition, polymer concentration, and water addition rate, we demonstrated precise control over nanoparticle morphology, enabling the formation of spherical micelles, worm-like micelles, and vesicles from a single polymer system. The results showed that even slight changes in these parameters significantly influence the final morphology of the nanoparticles.

The type of non-selective solvent emerged as the most critical parameter affecting particle shape. In this context, it is important to consider that the solvent's affinity for the hydrophobic core strongly influences both the core size and the degree of stretching of the hydrophobic block during the assembly process.[24] In this work, higher concentrations of DMSO favored the formation of vesicles, while balanced DMSO/acetone mixtures stabilized worm-like micelles. A higher acetone content led to the formation of spherical particles. An increase in polymer concentration generally resulted in larger particles, particularly vesicles. In contrast, lower concentrations led to the disappearance of the worm-like phase. The water addition rate had a pronounced effect on morphology evolution: faster addition (4 mL $h^{-1}$) broadened the worm-like phase. Interestingly, a very high water addition rate (20 mL $h^{-1}$) resulted in the formation of short worm-like micelles at DMSO contents below 50%, suggesting that turbulence and local inhomogeneities may play a role in early-stage aggregation. These effects may also contribute to the formation of mixed phases, which were frequently observed between pure morphologies. The free energy of two morphologies can be nearly equivalent, making subtle local differences sufficient to dictate the resulting structure.[42] Additionally, polymer dispersity may further contribute to the formation of different morphologies, as chains of varying length may transition to the next morphology at different times.[25]

These findings highlight the complex interplay of thermodynamic and kinetic factors in block copolymer self-assembly and underscore the potential of solvent switch techniques for designing shape-specific nanostructures. Notably, the obtained nanostructures remained stable for over a year, and even annealing at elevated temperatures did not induce morphological transitions, indicating that kinetic effects may play a decisive role in the assembly process. The work highlights that despite decades of research, several uncertainties remain regarding polymeric self-assembly in aqueous environments. However, the ability to target all major morphologies using a single block copolymer opens up exciting possibilities, particularly in applications such as nanomedicine, where nanoparticle morphology influences biodistribution, cellular uptake, and therapeutic efficacy.[21,54] Further experiments could show the influence of particle shape excluding all effects related to particle composition.

## Experimental part

### Materials and methods

All chemicals and solvents were purchased from Sigma-Aldrich, Acros Organics, Carl Roth, Merck, Jena Bioscience and were used without further purification unless mentioned otherwise. Pyridyldisulfide ethyl acrylate (PDSA) and 2-(butylthiocarbonothioylthio)propanoic hydroxysuccinimide (PABTC-NHS) were prepared *via* previously reported procedures.[61,62] 1,4-Dioxane and butyl acrylate (BA) were treated 24 h with inhibitor remover resin prior to use. $N_3\text{-}PEO_{125}\text{-}NH_2$ was purchased from Rapp Polymere.

DLS was performed on a ZetaSizer Nano ZS (Malvern, Herrenberg, Germany) equipped with a He–Ne laser operating at a wavelength of $\lambda = 633$ nm. Counts were detected at an angle of 173°. The particle size was approximated as the effective diameter (*Z*-average) obtained by the cumulants method assuming a spherical shape. All measurements were conducted at 25 °C in semi-micro cuvettes after equilibration times of 30 s in triplicate. Every measurement included 10 runs, in which every run took 30 seconds. Apparent hydrodynamic radii were calculated using the Stokes–Einstein equation (1):

$$R_\mathrm{h} = kT \cdot 6\pi\eta D \tag{1}$$

$R_\mathrm{h}$ = hydrodynamic radius, $k$ = Boltzmann constant, $T$ = absolute temperature, $\eta$ = viscosity of the sample, and $D$ = apparent translational diffusion coefficient.

AF4 measurements were performed on an AF2000 MT System from Postnova Analytics GmbH (Landsberg, Germany), equipped with a tip and focus pump (PN1130), an autosampler (PN5300), and a channel oven unit (PN4020) set to 25 °C. The channel was coupled to a multiangle laser light scattering (MALLS) detector (PN3621) equipped with a 532 nm laser and measuring 21 angles, a refractive index (RI) detector (PN3150), and a UV-detector (PN3212) set to 280 nm. The channel had a trapezoidal geometry with a nominal height of 350 µm. Regenerated cellulose (RC) membrane from Postnova Analytics GmbH (10 kDa RC membrane) with a molar mass cutoff of 10 kDa was used as accumulation wall. As the mobile phase aqueous solution with 0.02 wt% of $\mathrm{NaN_3}$ was used. 50 µL of the sample at a concentration of 1 mg $\mathrm{mL^{-1}}$ was injected with an injection flow rate of 0.2 mL $\mathrm{min^{-1}}$, a focus flow rate of 0.8 mL $\mathrm{min^{-1}}$, and a cross-flow rate of 0.7 mL $\mathrm{min^{-1}}$, resulting in a detector flow rate of 0.3 mL $\mathrm{min^{-1}}$. The focusing time was 4 min before switching to elution at an exponentially decaying crossflow from 0.7 mL $\mathrm{min^{-1}}$ to 0.2 mL $\mathrm{min^{-1}}$ in 76.2 min. Thereafter the crossflow profile was set to decay in a linear way from 0.05 mL $\mathrm{min^{-1}}$ to 0.04 mL $\mathrm{min^{-1}}$ in 71 min. Before the start of the next measurement, a rinsing step was performed at 1.5 mL $\mathrm{min^{-1}}$ flow of the tip pump for 20 min. After each sample measurement, a blank measurement was run which was subtracted from the data of the sample measurement for analysis. The MALLS data of the scattering angles from 20°–148° was analysed *via* ZIMM plot to obtain the radius of gyration ($R_\mathrm{g}$) at the specified elution times.

All Cryo-TEM measurements, exept Fig. 6b, were performed on a FEI Tecnai $\mathrm{G^2}$ 20 equipped with a $\mathrm{LaB_6}$ filament with an acceleration voltage of 200 kV. Samples were prepared on Quantifoil grids (R2/2) which were treated with Ar plasma prior to use for hydrophilization and cleaning. 8.5 µL of the solution were vitrified on Quantifoil grids using a Vitrobot Mark IV system. Liquid ethane was used as a cryogen. Samples were transferred to a Gatan 626 cryo holder and were maintained at a temperature <−175 °C during the entire process. All images were acquired with a Mega View (OSIS, Olympus Soft Imaging Systems) or an Eagle 4k CCD camera, respectively.

Cryo-TEM of Fig. 6b was performed on a JEOL JEM-2200FS operating at 200 kV and equipped with a field emission gun and an in-column energy omega filter. The zero-loss energy-filtered, bright field micrographs were recorded at cryo conditions (Holder $T = -174$ °C) with a bottom-mounted CMOS 4K camera (OneView, Gatan). The images were processed with digital processing software (Digital Micrograph 3.6, Gatan). For cryo preparation, 4 µL of the aqueous sample solution were deposited on a Cu grid with a holey carbon film (Quantifoil, Germany) that was glow-discharged before. The grid was then blotted at 15 °C and 90% humidity with filter paper and plunged into liquid ethane using a Leica EM GP plunge freezer (Leica, Germany). After preparation, the grids were stored and transferred to the TEM under liquid nitrogen.

Non-cryo-TEM investigations were conducted by blotting 15 µL of the solution (1 mg $\mathrm{mL^{-1}}$) onto freshly cleaned carbon support films (Quantifoil, Jena).

## Author contributions

The manuscript was written through contributions of all authors. All authors have given approval to the final version of the manuscript.

## Conflicts of interest

There are no conflicts of interest to declare.

## Data availability

The data supporting this article is presented in the main manuscript or have been included as part of the supplementary information (SI). Supplementary information is available and includes SEC and NMR data of the polymer, DLS data and AF4 elugrams of the assembled structures, as well as further TEM images. See DOI: https://doi.org/10.1039/d5py01038a.

## Acknowledgements

This work was financially supported by the DFG-funded Collaborative Research Centre PolyTarget (project-ID: 316213987 – SFB 1278; projects A05, C04, Z01). J. C. Brendel further thanks the DFG for funding within the Emmy-Noether Programme (project-ID: 358263073) and the Heisenberg-Programme (project-ID: 517761335). Cryo-TEM investigations were conducted at (i) the Jena Center for Soft Matter (JCSM) electron microscopy facilities established with funds by the DFG and the European Funds for Regional development (EFRE) and (ii) at the Keylab Electron and Optical Microscopy within the Bavarian Polymer Institute. We further gratefully acknowledge the support of Ivo Nischang and his team in performing the AF4 measurements.

## References

1 K. Matyjaszewski and A. H. Müller, *Controlled and living polymerizations: from mechanisms to applications*, John Wiley & Sons, 2009.
2 F. H. Schacher, P. A. Rupar and I. Manners, *Angew. Chem., Int. Ed.*, 2012, **51**, 7898–7921.
3 A.-L. Buckinx, L. J. Weerarathna, A. Sokolova and T. Junkers, *Polym. Chem.*, 2024, **15**, 4615–4621.
4 A.-L. Buckinx, K. Verstraete, E. Baeten, R. F. Tabor, A. Sokolova, N. Zaquen and T. Junkers, *Angew. Chem., Int. Ed.*, 2019, **58**, 13799–13802.
5 J. Jennings, G. He, S. M. Howdle and P. B. Zetterlund, *Chem. Soc. Rev.*, 2016, **45**, 5055–5084.
6 H. Dau, G. R. Jones, E. Tsogtgerel, D. Nguyen, A. Keyes, Y.-S. Liu, H. Rauf, E. Ordonez, V. Puchelle, H. Basbug Alhan, C. Zhao and E. Harth, *Chem. Rev.*, 2022, **122**, 14471–14553.
7 G. Theodosopoulos and M. Pitsikalis, *Block Copolymers by Anionic Polymerization: Recent Synthetic Routes and Developments*, Springer Japan, Tokyo, 2015.
8 S. E. Webber, *J. Phys. Chem. B*, 1998, **102**, 2618–2626.
9 K. Mori, H. Hasegawa and T. Hashimoto, *Polymer*, 1990, **31**, 2368–2376.
10 H. W. Deckman, J. H. Dunsmuir, S. Garoff, J. A. McHenry and D. G. Peiffer, *J. Vac. Sci. Technol., B: Microelectron. Process. Phenom.*, 1988, **6**, 333–336.
11 E. Blasco, M. B. Sims, A. S. Goldmann, B. S. Sumerlin and C. Barner-Kowollik, *Macromolecules*, 2017, **50**, 5215–5252.
12 M. Karayianni and S. Pispas, *J. Polym. Sci.*, 2021, **59**, 1874–1898.
13 P. Maji and K. Naskar, *J. Appl. Polym. Sci.*, 2022, **139**, e52942.
14 M. Hasannia, A. Aliabadi, K. Abnous, S. M. Taghdisi, M. Ramezani and M. Alibolandi, *J. Controlled Release*, 2022, **341**, 95–117.
15 C. Barner-Kowollik, A. S. Goldmann and F. H. Schacher, *Macromolecules*, 2016, **49**, 5001–5016.
16 C. M. Bates and F. S. Bates, *Macromolecules*, 2017, **50**, 3–22.
17 F. S. Bates and G. H. Fredrickson, *Phys. Today*, 1999, **52**, 32–38.
18 U. Tritschler, S. Pearce, J. Gwyther, G. R. Whittell and I. Manners, *Macromolecules*, 2017, **50**, 3439–3463.
19 J. C. Brendel and F. H. Schacher, *Chem. – Asian J.*, 2018, **13**, 230–239.
20 J. Chen, N. E. Clay, P. No-hyung and H. Kong, *Chem. Eng. Sci.*, 2015, **125**, 20–24.
21 E. Gardey, J. Eberhardt, S. Hoeppener, F. H. Sobotta, J. C. Brendel and A. Stallmach, *Macromol. Biosci.*, 2024, **24**, 2400179.
22 Y. Zhou, D. Gao, Y. Wang, L. Liang, Q. Zhang, W. Han, J. Wang, C. Zhu, X. Zhang and Y. Gan, *Chin. Chem. Lett.*, 2024, **35**, 108967.
23 M. Elsabahy and K. L. Wooley, *Chem. Soc. Rev.*, 2012, **41**, 2545–2561.
24 Y. Mai and A. Eisenberg, *Chem. Soc. Rev.*, 2012, **41**, 5969–5985.
25 O. Terreau, L. Luo and A. Eisenberg, *Langmuir*, 2003, **19**, 5601–5607.
26 N. J. W. Penfold, J. Yeow, C. Boyer and S. P. Armes, *ACS Macro Lett.*, 2019, **8**, 1029–1054.
27 A. Blanazs, A. J. Ryan and S. P. Armes, *Macromolecules*, 2012, **45**, 5099–5107.
28 F. H. Sobotta, M. T. Kuchenbrod, C. Grune, D. Fischer, S. Hoeppener and J. C. Brendel, *Polym. Chem.*, 2021, **12**, 1668–1680.
29 J. N. Israelachvili, *Intermolecular and Surface Forces*, Academic Press, San Diego, 3rd edn, 2011.
30 R. Nagarajan, *Adv. Colloid Interface Sci.*, 2017, **244**, 113–123.
31 S. L. Canning, G. N. Smith and S. P. Armes, *Macromolecules*, 2016, **49**, 1985–2001.
32 M. J. Derry, L. A. Fielding and S. P. Armes, *Prog. Polym. Sci.*, 2016, **52**, 1–18.
33 T. Nicolai, O. Colombani and C. Chassenieux, *Soft Matter*, 2010, **6**, 3111–3118.
34 C. J. Martínez Rivas, M. Tarhini, W. Badri, K. Miladi, H. Greige-Gerges, Q. A. Nazari, S. A. Galindo Rodríguez, R. Á. Román, H. Fessi and A. Elaissari, *Int. J. Pharm.*, 2017, **532**, 66–81.
35 H. Fessi, F. Puisieux, J. P. Devissaguet, N. Ammoury and S. Benita, *Int. J. Pharm.*, 1989, **55**, R1–R4.
36 G. Bovone, L. Cousin, F. Steiner and M. W. Tibbitt, *Macromolecules*, 2022, **55**, 8040–8048.
37 Y. Yu and A. Eisenberg, *J. Am. Chem. Soc.*, 1997, **119**, 8383–8384.
38 A. Sorrenti, J. Leira-Iglesias, A. J. Markvoort, T. F. A. de Greef and T. M. Hermans, *Chem. Soc. Rev.*, 2017, **46**, 5476–5490.
39 L. Zhang and A. Eisenberg, *Macromolecules*, 1999, **32**, 2239–2249.
40 L. Zhang and A. Eisenberg, *Science*, 1995, **268**, 1728–1731.
41 Y. Yu, L. Zhang and A. Eisenberg, *Macromolecules*, 1998, **31**, 1144–1154.
42 H. Shen and A. Eisenberg, *J. Phys. Chem. B*, 1999, **103**, 9473–9487.
43 A. Choucair and A. Eisenberg, *Eur. Phys. J. E*, 2003, **10**, 37–44.
44 K. Yu and A. Eisenberg, *Macromolecules*, 1998, **31**, 3509–3518.
45 X. Liu and I. Gitsov, *Macromolecules*, 2019, **52**, 5563–5573.
46 M. P. Vena, D. de Moor, A. Ianiro, R. Tuinier and J. P. Patterson, *Soft Matter*, 2021, **17**, 1084–1090.
47 N. P. Truong, J. F. Quinn, M. V. Dussert, N. B. T. Sousa, M. R. Whittaker and T. P. Davis, *ACS Macro Lett.*, 2015, **4**, 381–386.
48 H. Cui, Z. Chen, S. Zhong, K. L. Wooley and D. J. Pochan, *Science*, 2007, **317**, 647–650.
49 A. H. Gröschel, A. Walther, T. I. Löbling, F. H. Schacher, H. Schmalz and A. H. E. Müller, *Nature*, 2013, **503**, 247–251.

50 R. J. Carrazzone, X. Li, J. C. Foster, V. V. S. Uppala, C. E. Wall, A. R. Esker, L. A. Madsen and J. B. Matson, *Macromolecules*, 2021, **54**, 6975–6981.

51 S. Jain and F. S. Bates, *Macromolecules*, 2004, **37**, 1511–1523.

52 Y.-Y. Won, H. T. Davis and F. S. Bates, *Macromolecules*, 2003, **36**, 953–955.

53 M. Jacquin, P. Muller, R. Talingting-Pabalan, H. Cottet, J. F. Berret, T. Futterer and O. Théodoly, *J. Colloid Interface Sci.*, 2007, **316**, 897–911.

54 E. Gardey, Z. Cseresnyes, F. H. Sobotta, J. Eberhardt, D. Haziri, P. C. Grunert, M. T. Kuchenbrod, F. V. Gruschwitz, S. Hoeppener, M. Schumann, N. Gaßler, M. T. Figge, A. Stallmach and J. C. Brendel, *Small*, 2024, **20**, 2306482.

55 E. Gardey, F. H. Sobotta, S. Hoeppener, T. Bruns, A. Stallmach and J. C. Brendel, *Biomacromolecules*, 2020, **21**, 1393–1406.

56 M. Elsabahy, S. Samarajeewa, J. E. Raymond, C. Clark and K. L. Wooley, *J. Mater. Chem. B*, 2013, **1**, 5241.

57 F. V. Gruschwitz, T. Klein, M. T. Kuchenbrod, N. Moriyama, S. Fujii, I. Nischang, S. Hoeppener, K. Sakurai, U. S. Schubert and J. C. Brendel, *ACS Macro Lett.*, 2021, **10**, 837–843.

58 E. G. Kelley, R. P. Murphy, J. E. Seppala, T. P. Smart, S. D. Hann, M. O. Sullivan and T. H. Epps, *Nat. Commun.*, 2014, **5**, 3599.

59 J. van Stam, S. Creutz, F. C. De Schryver and R. Jérôme, *Macromolecules*, 2000, **33**, 6388–6395.

60 M. Fauquignon, L. Porcar, A. Brûlet, J.-F. Le Meins, O. Sandre, J.-P. Chapel, M. Schmutz and C. Schatz, *ACS Macro Lett.*, 2023, **12**, 1272–1279.

61 B. Remant, B. Thapa and P. Xu, *Mol. Pharm.*, 2012, **9**, 2719–2729.

62 S. Larnaudie, J. Brendel, K. Jolliffe and S. Perrier, *J. Polym. Sci., Part A: Polym. Chem.*, 2016, **54**, 1003–1011.